Model-Chain Validation for Estimating the Energy Yield of Bifacial Perovskite/Silicon Tandem Solar Cells

Peter Tillmann, Klaus Jäger, Asher Karsenti, Lev Kreinin, and Christiane Becker*

The power conversion efficiency of conventional silicon solar cells approaches its theoretical limit. Bifacial operation and the perovskite/silicon tandem device architecture are promising approaches for increasing the energy yield of photovoltaic modules. Here, an energy yield calculation tool for (bifacial) perovskite/silicon tandem solar cells is presented. It uses a chain of models for irradiance, optical absorption, and temperature-dependent electrical performance. Each step is validated with irradiance and performance data from a rooftop installation with mono- and bifacial silicon solar cells in Jerusalem, Israel. Selecting the data for two days (one in summer, one in winter) and considering the high-reflective ground of this particular installation (albedo 60%) a 20% increased energy yield for a bifacial module with respect to a monofacial module is modeled. This result matches well with experimental data. When "upgrading" the silicon solar cell to a perovskite/silicon tandem solar cell, the case study predicts up to 40% additional energy yield. Combining the concepts of bifacial solar operation and perovskite/silicon tandem solar cells results in up to 60% increased energy with a high albedo ground, and is therefore a promising approach to further decrease the levelized cost of electricity for photovoltaic electricity generation.

1. Introduction

The market share of bifacial photovoltaic (PV) modules has grown remarkably in recent years. Bifacial modules not only utilize light impinging onto the front side of the PV module, but also light reaching the backside.[1,2] The International

P. Tillmann, K. Jäger, C. Becker
Department Optics for Solar Energy
Helmholtz-Zentrum Berlin für Materialien und Energie
12489 Berlin, Germany
E-mail: christiane.becker@helmholtz-berlin.de

P. Tillmann, K. Jäger
Computational Nano Optics
Zuse Institute Berlin
14195 Berlin, Germany

A. Karsenti, L. Kreinin
Lev Academic Center
SolAround Ltd.
Jerusalem 9611001, Israel

The ORCID identification number(s) for the author(s) of this article can be found under https://doi.org/10.1002/solr.202200079.

Technology Roadmap for Photovoltaics revised the prediction on market share for bifacial cell technology for a certain date upwards year by year and meanwhile predicts a share of more than 75% bifacial cells in 2031.[3] Particularly passivated emitter rear cell (PERC) and rear totally diffused (PERT) silicon cells allow for bifacial operation, and hence more power generation at nearly zero additional costs. This enables the reduction of the levelized cost of electricity (LCOE) at a fast pace[4] and opens up new application fields such as agricultural PV[5] and floating PV.[6]

Accurate modeling of the energy yield of bifacial solar power plants is of utmost importance as it allows to estimate the LCOE at a certain location, which is a crucial figure-of-merit to judge the bankability of planned solar power plants. Modeling the energy yield from monofacial solar modules based on weather data, such as direct and diffuse solar irradiance, temperature, wind speed, and the geometrical arrangement and surroundings of the module, has been well-developed in the past decades. However, modeling the rear-side irradiance on a solar module is still regarded as challenging,[7] particularly on so-called "variable" days with quickly changing cloud coverage, and more general, on shorter time scales.[8] The reason is that the rear side of a solar module mainly receives light reflected from the ground with a timely variable pattern of directly illuminated and shadowed areas seeing more or less from the diffuse skylight. In 2019, Pelaez et al. compared five different bifacial illumination models[9] either based on ray tracing,[10] a view factor model,[11] or an empirical model based on a large amount of field data,[12] all predicting the front and irradiance on sunny days within reasonable errors. However, when taking the next step toward multijunction solar cells one has to look more closely and accurate modeling of bifacial irradiance at short time scales becomes even more important.

In case of two-terminal tandem devices, which are the preferred configuration in terms of minimized balance-of-system costs and low parasitic absorption losses in contact layers, current matching is required for maximal power output. Both, the PV system and the solar cells, have to be designed in such a way that an equal number of photons is absorbed in the top and bottom cells, respectively, because otherwise the whole device is limited by the subcell absorbing fewer photons. While variable weather conditions tend to average out in bifacial single-junction devices, variations of front and rear side illumination can significantly

disturb current-matching in bifacial tandem solar cells.[13] Various theoretical energy-yield calculation models were developed for the currently widely discussed two-terminal perovskite/silicon tandem solar cells[14] in bifacial operation.[13,15–18] However, only very little experimental data of bifacial two-terminal perovskite/silicon tandem solar cells on outdoor test fields have been published so far.[19] Hence, in the medium term, the prediction of the energy yield of this technology will still rely on simulations. More important is to validate the rear-side illumination models by experimental field data, e.g., from bifacial silicon single-junction solar cells at the specific location of interest, to enable reasonable predictions for bifacial tandem solar cells as well.

In this study, we combine several models to calculate the energy yield of the investigated devices. Each step in the chain of models is validated with data from a mono- and a bifacial silicon solar module. In the first step, we apply an illumination model for bifacial solar modules arranged as an infinitely extended array based on view-factor considerations.[20] We compare the simulations with the measured data from a bifacial solar cell module installed in a small power plant located on a rooftop in Jerusalem, Israel, on two sunny days (one in winter and one in summer) as well as one "variable" day with quickly changing cloud coverage. Comparing the measured generated current with the modeled combined irradiance from the front and rear sides of the module allows to validate the optical view factor model nearly independently from module temperature and wind speed. In a second step, we implement a temperature-dependent electrical model to compare measured and simulated generated power. Finally, we use our validated bifacial solar cell model to predict the energy yield of perovskite/silicon tandem solar cells with the perovskite top cell on the front side, and also the configuration with perovskite cells "sandwiching" the silicon bottom cell on both, front and rear side.

2. Experimental Data and Numerical Methods

2.1. Experimental Data Basis

The experimental data used in this work was recorded on a rooftop installation in Jerusalem, Israel, provided by SolAround Ltd. **Figure 1**a shows the rooftop installation, made of four rows of solar panels mounted in landscape orientation with three panels per row. A high-albedo plastic foil under the solar panels is used to increase the amount of light reflected onto the back side of the modules. The installation includes mono- and bifacial modules and sensors for measuring the global, diffuse and direct irradiance. K-type thermocouples are installed at the back side of solar panels to measure the cell temperature. The temperature sensor should give a good estimate of the operation conditions of the solar cells, but the actual cell temperature is likely slightly higher than the temperature measured at the back side of the panel. From the solar panels, the short-circuit current (I_{SC}), open-circuit voltage (V_{OC}), maximum power, and fill factor (FF) are measured each minute. Three days of data are available, August 26, 2019 (sunny summer day), February 15, 2020 (sunny winter day), and February 19, 2020 (cloudy/variable winter day). The parameters used to represent the rooftop installation are summarized in **Table 1**.

2.2. Numerical Methods

2.2.1. Bifacial Illumination Model

The first step to calculate the characteristics of the bifacial solar cells is to simulate the irradiance on the front and back sides. For the irradiance simulation, we employ a recently developed view factor illumination model,[20,21] which was specifically designed for bifacial solar cells. In that model, the PV field is considered so large that boundary effects can be neglected. The geometry of the solar panels is simplified (the panels are assumed to be perfectly flat, with no frame) and the front and back side are modeled as perfectly black. These assumptions are used in many view-factor models and typically lead to an underestimation of the back side irradiance of 5–20%.[22,23] Figure 1b shows the schematic illustration of the components reaching the module front and back each: direct sunlight, diffuse skylight, diffuse light from the ground originating from direct sunlight reaching the ground, and diffuse light from the ground originating from diffuse skylight reaching the ground. To describe the geometry of the PV installation under investigation the model requires the module length ℓ, mounting height h, module spacing d, and tilt angle θ_m. Second, also the albedo (i.e., the reflectivity) of the ground is required (see Table 1).

For the rooftop location in Jerusalem, no spectrally resolved solar irradiance data is available. However, broadband direct and diffuse irradiance are measured by pyranometers with a time resolution of one minute. To emulate the spectral information
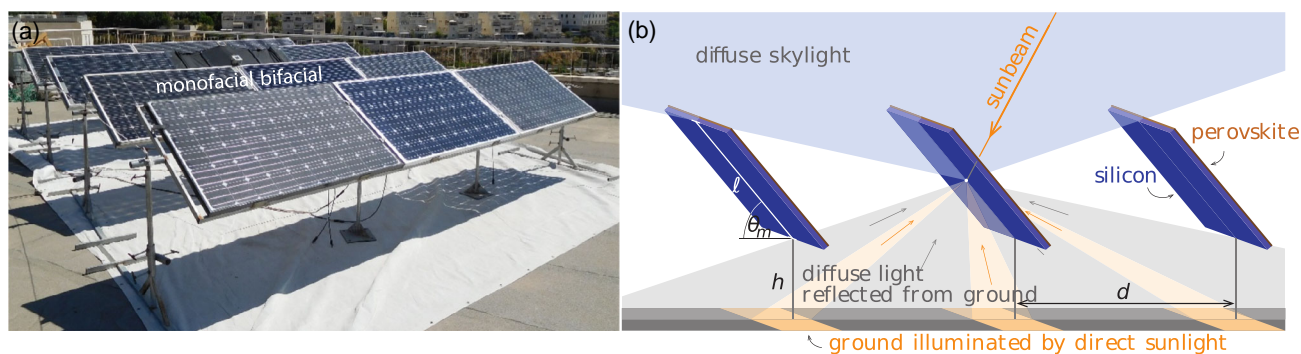

Figure 1. a) Photograph of the mono- and bifacial silicon solar panel rooftop installation located in Jerusalem, Israel, delivering the experimental data for model validation. All data for monofacial cells is measured with the left module in the second row, bifacial data is measured with the module in the middle of the second row. b) Schematic representation of the bifacial irradiance model used in this study. Adapted under terms of the CC-BY license.[18] Copyright 2021, The Authors. Solar RRL published by Wiley-VCH GmbH.

Table 1. Experimental parameters of the solar panel rooftop installation in Jerusalem.

Model parameters			
ℓ	module length [m]		1.0
d	module spacing [m]		1.9
h	module height above the ground [m]		0.8
θ_m	module tilt angle		30°
A	albedo of the ground		60%
Solar cell parameters at standard test conditions (STC)			
Front-side illumination			
V_{OC}	Open-circuit voltage [V]		38.8
I_{SC}	Short-circuit current [A]		9.83
FF	FF [%]		74
P	Power [W]		283
Rear-side illumination			
V_{OC}	Open-circuit voltage [V]		38.6
I_{SC}	Short-circuit current [A]		8.35
FF	FF [%]		74
P	Power [W]		242
	Bifaciality (Ratio rear to front power)		85%
	Number of cells per module		60
	Cell active area (unshaded by wires) [cm^2]		240
Outdoor solar panel field data			
V_{OC}	Open-circuit voltage [V]		
I_{SC}	Short-circuit current [A]		
FF	FF [%]		
P	Power at maximum power point [W]		
Measured solar and temperature data			
DHI	Diffuse horizontal irradiance [W m^2]		K&Z CMP11 Pyranometer with shadow ring
GHI	Global horizontal irradiance [W m^2]		K&Z CMP11 Pyranometer
POA	Irradiance in the plane of the module front side [W m^2]		Phox SOZ-03 silicon reference cell
T_c	Cell temperature		Type K thermocouple at back side of the module

needed to calculate the photocurrent we use spectrl2, a model based on radiative transfer simulations developed by Bird and Riordan.[24] spectrl2 calculates the direct and diffuse spectral irradiance based on the solar position and several atmospheric parameters, such as precipitable water, ozone concentration, and aerosol optical depth. This model is only suitable for clear-sky conditions and therefore only applicable for describing the two sunny days August 26, 2019 and February 15, 2020.

2.2.2. Optical Solar Cell Model

We use the MATLAB-based software package GenPro4[25] to calculate the optical absorption, reflection, and transmission of the investigated cell architectures. GenPro4 uses the

net-radiation method for multilayer stacks and ray tracing for simulating scattering by pyramidal interfaces. As input, we provide detailed layer stacks, the type of interface (planar or textured), and the complex refractive index (*nk*-data) for the used materials. All detailed layer stacks and references for the used *nk*-data are summarized in the Supporting Information (SI) Section S5.

To study how the perovskite bandgap affects the solar-cell performance, we performed a wavelength shift of the available *nk* dataset for perovskite.[26] This estimation is justified by experimental data.[27]

We calculated the photocurrent densities as functions of the absorption and the spectral irradiance using

$$J_{ph} = e \int_{300\,nm}^{1200\,nm} A(\lambda)\Phi_f(\lambda)d\lambda \tag{1}$$

where e is the elementary charge, $A(\lambda)$ is the absorption in the considered absorber layer, and Φ_f is the photon flux reaching the module. The photon flux can be calculated from the spectral irradiance according to

$$\Phi_f(\lambda) = E_\lambda \frac{\lambda}{hc} \tag{2}$$

with the spectral irradiance E_λ, the Planck constant h and the speed of light c.

2.2.3. Temperature-Dependent One-Diode Model

An electrical model is used to calculate the power output of a solar cell from the absorbed photocurrent. To get a realistic estimation of the power output different factors such as the electrical resistance and temperature have to be accounted for. In this work, we use a one-diode model to calculate the current–voltage characteristics (*IV*-curves) of each solar cell. The one-diode model assumes an equivalent circuit, where an ideal current source is connected in parallel to a diode and optionally one or two resistors to model the series and shunt resistance of the solar cell. We use the following equation in our work

$$J(V) = J_{ph} - J_0\left[\exp\left(\frac{V + J \cdot R_{series}}{kT/e}\right) - 1\right] - \frac{V + J \cdot R_{series}}{R_{shunt}} \tag{3}$$

with the dark saturation current density J_0, elementary charge e, the Boltzmann constant k, the temperature T, photon current density J_{ph}, series resistance R_{series}, and shunt resistance R_{shunt}. This form of the one-diode equation has three parameters that determine the *IV*-curve for a given illumination and temperature: series resistance, shunt resistance, and dark saturation current. These parameters can typically be extracted from the measured *IV*-curve by fitting the one-diode equation to match the experiment. While series and shunt resistance are only slightly dependent on temperature (we assume it to be constant for simplicity) the dark saturation current is strongly dependent on the temperature. Therefore, we are not fitting the dark saturation current directly. Using the integrated overlap of the blackbody radiation and the external quantum efficiency (EQE) of a junction an idealized but temperature-dependent dark saturation current can be computed[28,29]

$$J_{0,\text{ideal}}(T) = e \int_0^\infty \text{EQE}(\lambda)\Phi_{\text{BB}}(\lambda, T)\mathrm{d}\lambda \qquad (4)$$

with the elementary charge e and the photon flux of the black body radiation Φ_{BB}. Using arguments of reciprocity and considering the limited external quantum efficiency EQE_{el} of a real cell a realistic and temperature-dependent dark saturation current J_0 can be calculated.[28]

$$J_0(T) = \frac{J_{0,\text{ideal}}(T)}{\text{EQE}_{\text{el}}} \qquad (5)$$

For details of the approach please see Supporting Information Section S1. It should be noted that we assume a constant ideality factor for the diode of $n = 1$.

3. Results

3.1. Validation of the Bifacial Illumination Model

In a first step, we aim to validate the optical bifacial illumination model by comparing simulated with experimental data. The illumination model calculates the intensities of the direct and diffuse light that are received at the front and back side of the solar modules. While the illumination on the backside is not directly measured we can use the short-circuit current of a bifacial module as a proxy.

Figure 2a shows the dependence between the plane-of-array irradiance on the front side of the solar cell modules and the short-circuit current measured on a monofacial PERT silicon solar cell module. The plane-of-array irradiance is directly measured by a reference cell mounted in the same plane as the solar cell modules. The silicon solar module is rated for a short-circuit current I_{SC} of 9.83 A at standard testing conditions (STC), i.e., $1000\,\text{W m}^{-2}$ irradiance. The red line shows the linear dependence of the short-circuit current on the irradiance calibrated with the STC measurement. The blue dots represent the short-circuit current measured over the course of August 26, 2019 and February 15, 2020. This shows that the short-circuit current I_{SC} is an excellent proxy for the irradiance. Here, the data points from February 19, 2020 are excluded because the time-stamps of the irradiance and the short-circuit current are not perfectly aligned (in the temporal sense), and therefore can diverge considerably in rapidly changing cloud coverage.

Because of the nearly linear response of the short-circuit current with respect to the plane-of-array irradiance, we use a constant factor determined by the short circuit current measured at STC for the model validation of this section
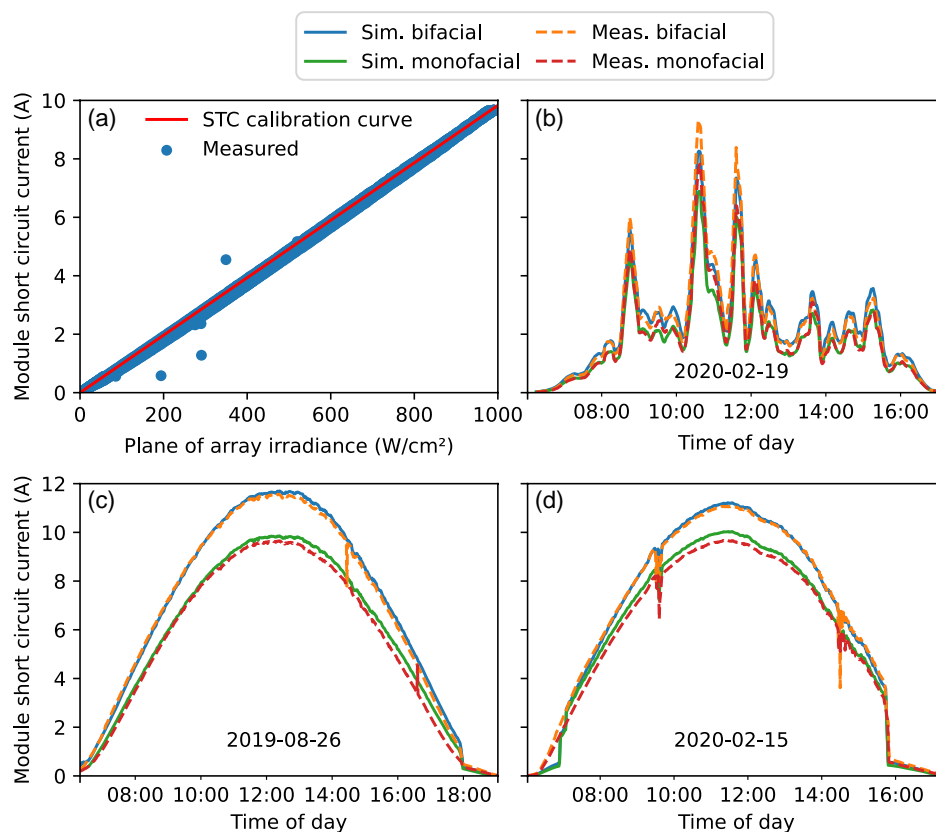

Figure 2. Validation of the bifacial illumination model. a) Correlation between measured module short-circuit current and measured plane of array irradiance (blue symbols), and calibration curve from solar cell characteristics at standard testing conditions (STC) (red line). b–d) Comparison of measured and modeled short-circuit current for mono- and bifacial solar modules at one variable day (b) and two sunny days (b),(c) by combining the bifacial irradiance model with the STC calibration curve. In part (b) a 15 min rolling average is shown. The output of the irradiance model depends on the DNI and DHI readings, position of the sun and the photovoltaic (PV) installation geometry detailed in Table 1.

$$J_{ph,front} = \frac{9.83A}{1000W} \cdot E_{front}$$

$$J_{ph,back} = \frac{8.35A}{1000W} \cdot E_{back} \qquad (6)$$

$$J_{ph,bifacial} = J_{ph,front} + J_{ph,back}$$

with E_{front} and E_{back} as the irradiance calculated by the irradiance model for the front and back side respectively. These calculations are based on the pyranometer readings for the DNI and DHI, as well as the position of the sun (in terms of azimuth and zenith angle) and the geometry of the PV installation detailed in Table 1.

Figure 2b–d shows the simulated and measured module short-circuit current for a bifacial and monofacial silicon module on August 26, 2019, February 15, 2020, and February 19, 2020, respectively. For the 2 days with clear-sky conditions, the calculated curves are very close to the measured lines, showing a good agreement between measurement and simulation. The variable day (February 19) is much more demanding. The results shown are 15 min rolling average because the very fast changes in irradiance otherwise would render the graphic unreadable. Because the timestamps of the irradiance are not perfectly aligned with the short-circuit current measurements some divergence between simulation (based on the irradiance) and measurement is to be expected. Also, the underlying assumption of the illumination model (all direct sunlight originates from a point source while the diffuse light is distributed isotropically over the hemisphere) is less valid for situations with rapidly changing cloud coverage. Nonetheless, the illumination model is still able to reproduce the general trends of the short-circuit current. However, some higher differences are visible between model and measurement, especially for times with high and quickly changing irradiance.

3.2. Validation of the Optical Solar Cell and Spectral Models

As detailed in Section 2.2, we use a three-step modeling approach to calculate the generated photocurrent density in each junction of the photovoltaic devices. First, we simulate the optical absorption profile of the investigated solar cell using the material stack as input. Second, we generate spectral information from broadband irradiance measurement and weight them with the results of the bifacial illumination model. Third, we combine spectral absorption and spectral irradiance to calculate the photocurrent density in the relevant junctions of the solar cell devices according to Equation (1).

Figure 3a shows the layer stack used for calculating absorption, reflection, and transmission of the bifacial SolAround PERT solar cell. The details of the layer stack and the used *nk*-data are found in the Supporting Information, Section S5. Figure 3b,c shows the result of the optical GenPro4 simulation with front side and back side illumination, respectively.

Figure 3d shows selected examples of the calculated spectral direct irradiance for different times on August 26, 2020. A spectrum according to AM1.5g is added as a reference. A red shift is clearly visible for the early morning spectrum at 7:10 am resulting from the increased scattering of short-wavelength light due to the prolonged light path through the atmosphere. At 8:50, the

spectrum is already close to the 10:30 and 12:10 spectra, which are very similar and nearly identical to the AM1.5 reference spectrum.

To compare the calculated photocurrent with the measured short-circuit current, the area of the solar cell and the number of cells in one module has to be considered. For a cell, we assume an active area (area of the cell that actively contributes to the absorption) of $240\,cm^2$ and 60 cells per module.

Figure 3e shows the photocurrent of the simulated mono- and bifacial PERT solar module and the measured short circuit current. Simulation and measurement are in good agreement and the results are very similar to the simulated short-circuit current based on STC measurements.

3.3. Validation of the Temperature-Dependent One-Diode Model

We use a one-diode model to calculate the *IV*-curves for a given temperature and absorbed photocurrent. From the *IV*-curve the open-circuitvoltage, FF, and maximum power point are derived. The details of the model are described in the numerical method section above. The measured values for V_{OC} and *FF* of silicon PERT solar cells mounted at the rooftop installation were fitted to acquire the necessary parameters for the one-diode model. We found $R_{series} = 1.9\,\Omega\,cm^2$, $R_{shunt} = 1000\,\Omega\,cm^2$ and $EQE_{el} = 0.16\%$.

Both the open-circuit voltage and the *FF* strongly depend on the temperature according to the one diode model (see Figure S4 in the Supporting Information). The level of irradiance also influences the *FF* and open-circuit voltage. Higher levels of irradiance have a positive impact on the open-circuit voltage while the *FF* has a peak, depending on the series and shunt resistance of the cell. Higher temperatures always reduce *FF* and open-circuit voltage. A more detailed discussion of these effects is given in the Supporting Information, Section S3.

Figure 4 shows the measured module temperature (T_m) and global horizontal irradiance (GHI) (a), the measured and simulated power output P (b), the *FF* (c), and the open-circuit voltage V_{OC} (d). Overall measured and simulated parameters of the solar cell agree very well. Over the course of the morning temperature and irradiance gradually increase. While the increasing irradiance leads to increasing V_{OC} higher cell temperatures reduces it. These competing trends of temperature and irradiance on the *FF* and V_{OC} are well reproduced by the model and result in good agreement for the power simulation of the solar cell modules. Larger differences are found only for very low levels of light intensity in the morning and times when either the irradiance sensor and/or the solar panels are shaded in the evening. This confirms that the chosen simulation approach is well suited to reproduce the measured power output of the silicon based PERT modules produced by SolAround. In Section S3.1 of the Supporting Information, we show the results for the simulation of the bifacial solar cell and discuss the differences for modeled and simulated results. The main differences between results for the bifacial and monofacial solar cells are an unexpected high *FF* measured for the bifacial solar cell when using the same cell parameters as used for the monofacial cells. We additionally benchmarked a two-diode model assuming a constant,
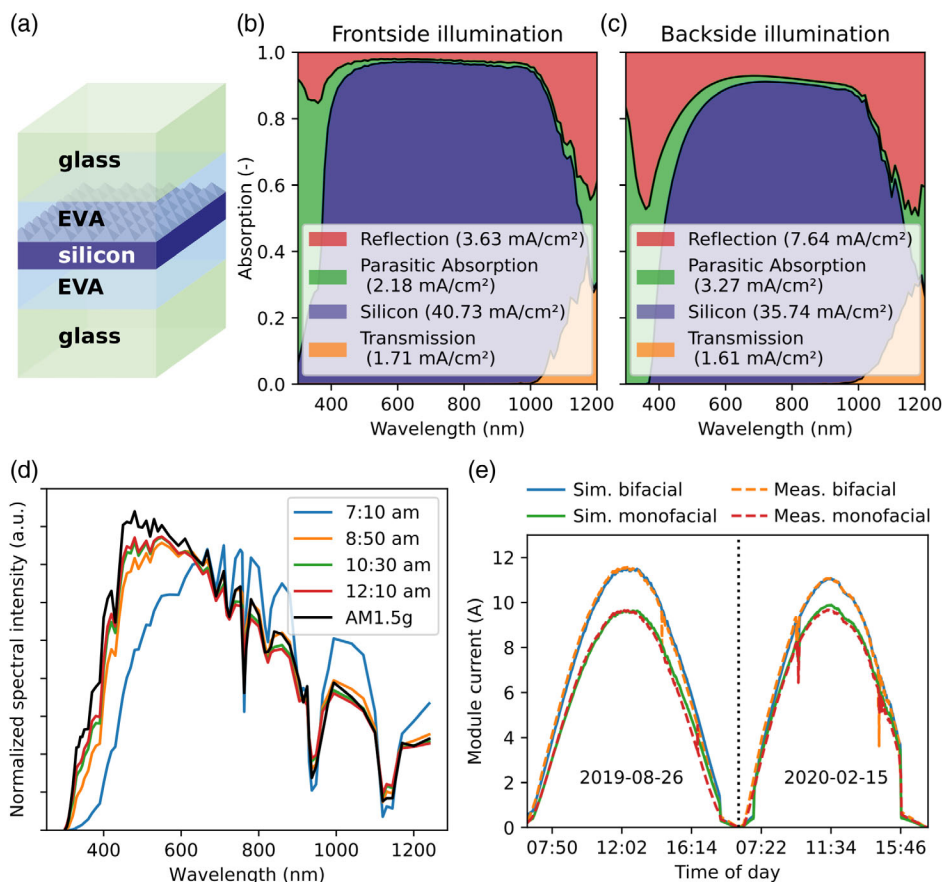
Figure 3. Validation of optical solar cell modelling. a) Layer stack of the frontside textured passivatated rear totally diffused (PERT) bifacial solar cells used to simulate absorptance, transmittance and reflectance for b) frontside and c) back side illumination with the software GenPro4. For a better clarity, the thin contact, passivation and doping layers or not show here; the respective parasitic absorption is summarized in green in part (b) and (c). The detailed layer stack can be found in the Supporting Information Section S5. d) Examples of modeled spectral direct normal irradiance according to the model spectrl2[24] for different times on August 26, 2020 and AM1.5g spectrum for comparison. e) Comparison of measured and modeled short-circuit current for mono- and bifacial solar modules on two sunny days by combining the bifacial irradiance model (separately validated in Figure 2), spectrl2 and optical simulations using GenPro4.

temperature-independent dark saturation current for the second diode. The parameters were fitted for a JV curve recorded under STC and results are shown in S2 and S3 in the Supporting Information. Due to the ambivalent results from the comparison of the one- and two-diode model we used the simpler one-diode model for the remainder of this work.

3.4. Energy Yield Predictions for Bifacial Perovskite/silicon Tandem Solar Cells

In this section, we estimate the energy yield that would be obtained if the bifacial solar panel array located on a rooftop in Jerusalem, Israel, did not consist of mono- or bifacial silicon solar modules, but of perovskite/silicon tandem solar cells of different configurations. We introduce 2- and 4-terminal connected perovskite-on-silicon tandem solar cells, simulate the 2-day energy yield for bifacial and monofacial devices and discuss the effects of the perovskite bandgap. Later in this section, we propose a 4-terminal architecture with three junctions, two

perovskite junctions surrounding a silicon junction in the middle, like a "sandwich," and discuss its performance prospects.

Figure 5 illustrates the 2-terminal connected and 4-terminal connected tandem solar cells. The solar cell stack for 2-terminal connected tandem solar cells is based on work by Al-Ashouri et al.[14] that marks the highest perovskite/silicon tandem solar cell efficiency with published details of the layer stack. These tandem cells use a MeO-2PACz self-assembled monolayer (SAM) as selective contact for hole transport. This layer is shown for completeness in Figure 5 but it is not considered in the optical simulation because it is unlikely to affect the optical response due to its very small thickness (1–2 nm). Here we focus on tandem solar cells where the perovskite cell is processed on the polished side of the silicon bottom cell and the textured side facing downwards. This approach enables spin-coating deposition of the top cell, which shows the highest efficiencies published so far.[14] From an industrial manufacturing point of view, double-sided textured silicon bottom cells might be favorable in the future[30–32] and our modeling approach is fully applicable to these kinds of cell technologies as well.[33]
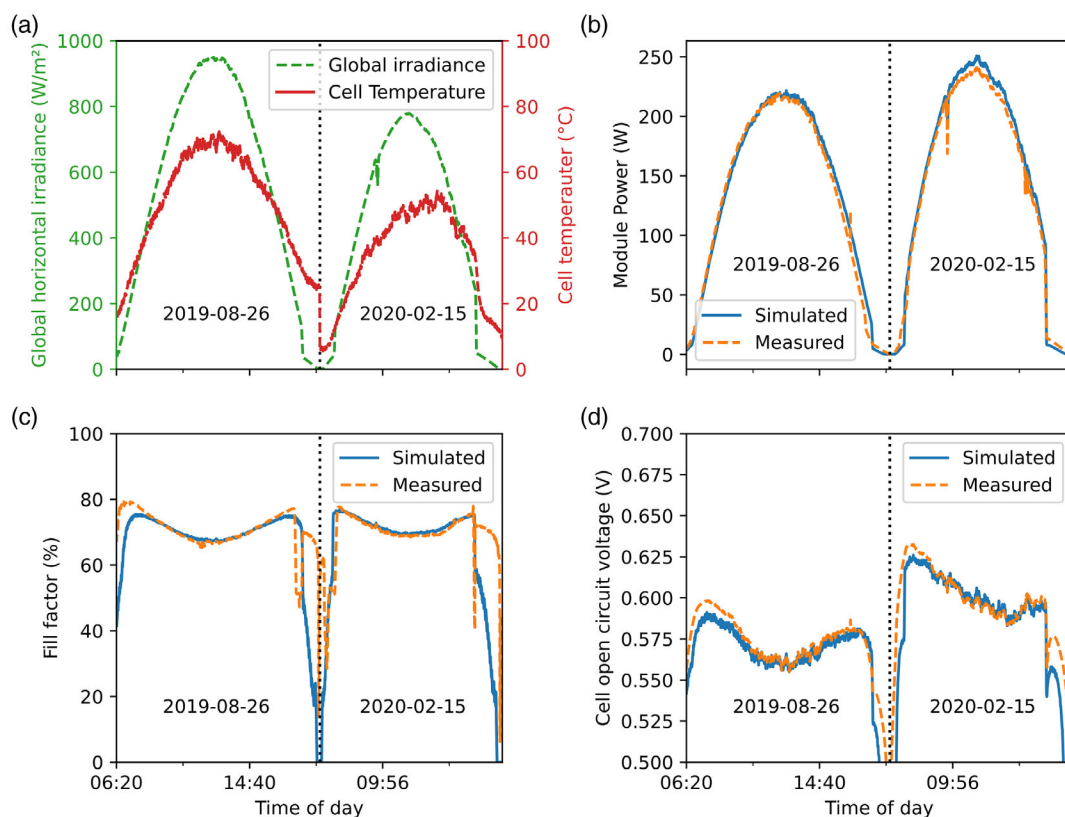
Figure 4. Measured sensor data and parameters of monofacial solar cells over the course of August 26, 2019 and February 15, 2020. a) Measured global horizontal irradiance and cell temperature. Comparison of simulated (one-diode model) and measured b) module power, c) fill factor (FF), and d) open-circuit voltage.
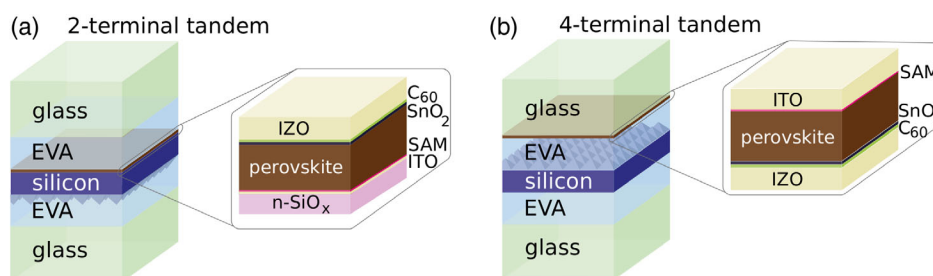

Figure 5. Schematic of the simulated bifacial tandem stack in a) 2-terminal and b) 4-terminal configuration. One side of the silicon exhibits a pyramidal texture, the other side is planar. In the case of the 2-terminal tandem the perovskite is assumed to be processed on the planar side of the silicon bottom cell while in the 4-terminal configuration the texture is pointed upwards to minimize reflection losses under top illumination. The self-assembled monolayer (SAM) is shown for completeness but ignored in the optical simulations due to its very small thickness (1–2 nm). The detailed stacks including all considered interlayers can be found in Supporting Information Section S5.

In this study, we adapt the silicon bottom cell architecture and use cell parameters of the SolAround solar cells. The PERT cells from SolAround are based on p-type silicon wafers and textured at the front side. For the simulation of tandem stacks a silicon oxide interlayer was added (shown as n-SiO$_x$ in the layer stacks). This silicon oxide interlayer is highly doped (for electrical conductivity) and was used by Al-Ashouri et al. to reduce the reflection between the perovskite and silicon subcell.

For the cell parameters of the perovskite subcell (EQE$_{el}$, R_{shunt}, R_{series}) we fit results published by Jošt et al.[34] on the temperature dependence of the efficiency and V_{OC} of the perovskite solar cell. Details of the fitting results can be found in the Supporting Information Section S4.

For the 4-terminal tandem, we assume a stack consisting of a perovskite top cell as used by Jošt et al. processed on the front glass and, separated by a layer of EVA, the silicon bottom cell

with the textured side to the front. The copper contact of the perovskite is replaced with a 200 nm thick layer of indium zinc oxide (IZO) for transparency in the infrared region. This approach likely leads to a too optimistic estimation of the performance of the 4-terminal tandem cell because the lateral current flow through the IZO layer will cause a higher series resistance compared to the copper contact of the reference. However, we do not account for this difference because it is not quantitatively accessible.

All fitted values for EQE_{el} and resistivity for the 2- and 4-terminal configurations are summarized in **Table 2**. The details of the stacks with all relevant interlayers (transparent conductive oxides, charge carrier transport layers, anti-reflective coatings)

and the corresponding absorption spectra calculated with GenPro4 are found in the Supporting Information, Section S5. The generated photocurrent density in the silicon and perovskite junctions is in line with state-of-the-art 2-terminal[14] and 4-terminal[35] perovskite on silicon tandem cells. However, the power conversion is 3–4 percentage points (p.p.) below the values reported in these research articles. This is mainly due to the usage of silicon cell parameters of solar modules produced with standard industrial processes while research articles often use high-end silicon cells that are only available on small scales. Also, the parameters for the perovskite cell correspond to a lower efficiency then would be found for small-scale record cells.

For all simulations of tandem solar cells, we assume that the modules are mounted in the same rooftop installation shown in Figure 1 with the geometry detailed in Table 1 and the same albedo of 60%. **Figure 6** shows the calculated photocurrent density generated in the $(a + c)$ perovskite and $(b + d)$ silicon junction in a bifacial (top row) and a monofacial (bottom row) tandem for different perovskite bandgaps. Overall the photocurrent density follows the irradiance over the course of the day with the highest levels around midday. Decreasing the perovskite bandgap increases the photocurrent density because more photons with energies above the bandgap can be utilized. As a consequence, the photocurrent density in the silicon junction decreases with lower perovskite bandgaps. While the perovskite junction is unchanged for mono- or bifacial operation the silicon junction generates significantly higher current densities with
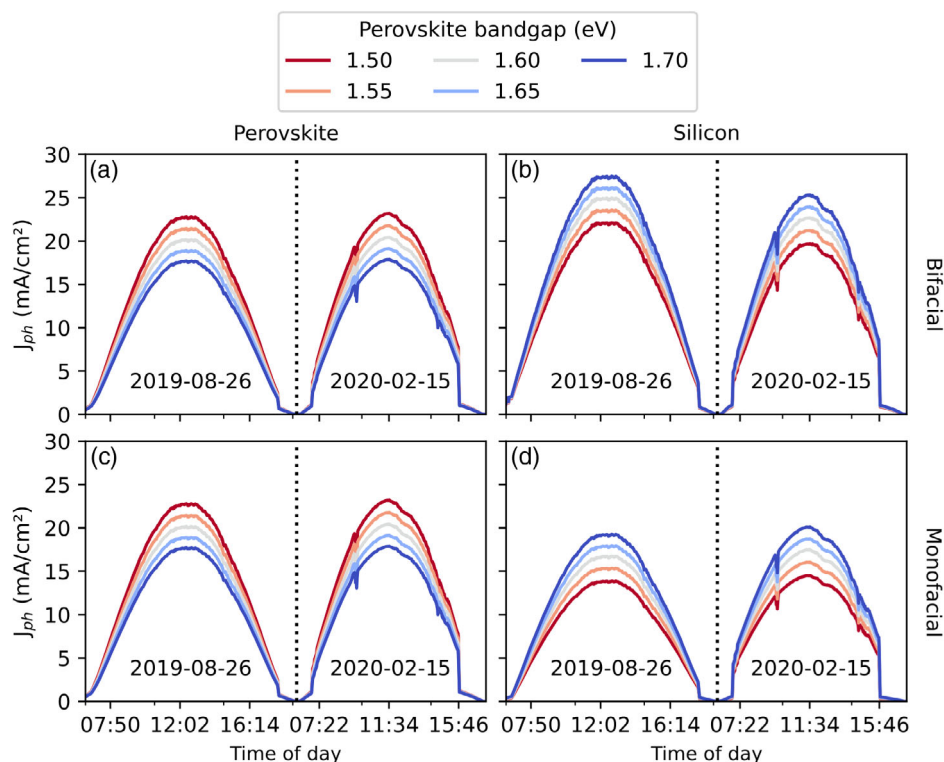
Table 2. Summary of the fitted cells parameters (R_{series}, R_{shunt}, and EQE_{el}) for different cell types and simulation results (η, V_{oc}, and J_{ph}) for standard testing conditions (25 °C, AM1.5g illumination). Where appropriate separate values for top and bottom cells of the tandems have been indicated with top cell value/bottom cell value.

	R_{series} [$\Omega\,cm^2$]	R_{shunt} [$\Omega\,cm^2$]	EQE_{el} [%]	η_{STC} [%]	V_{oc} [V]	J_{ph} [mA cm^{-2}]
Silicon	1.9	1000	0.16	19.3	0.655	40.7
Perovskite	6	1000	0.12	18.3	1.103	22.1
T tandem	6	1000/1000	0.16/0.12	25.3	1.735	18.8
T tandem	6/1.9	1000/1000	0.16/0.12	24.9	1.114/0.619	19.9/17.5

Figure 6. Absorbed photocurrent density J_{ph} of the (left) perovskite and (right) silicon subcell of 2-terminal perovskite/silicon tandem solar cells over the course of 26 August 2019 and 15 February 2020. The upper row (a,b) and lower rows (c,d) show results for a bifacial and for a monofacial tandem device, respectively. The geometrical parameters of the solar panel array as well as the albedo (60%) are identical to the parameters of the Jerusalem rooftop installation as specified in Table 1.

back side illumination. The light reaching the back of the bifacial tandem is exclusively absorbed in the silicon cell. This is because silicon has a lower bandgap than perovskite. All light that is transmitted because of photon energies below the bandgap of the silicon is also below the bandgap of the perovskite and therefore can not be absorbed there either.

With a perovskite bandgap of 1.55 eV the bifacial device generates roughly the same photocurrent density in the perovskite and silicon junctions and hence is at current-matching conditions. For the monofacial tandem solar cell, the optimal perovskite bandgap is significantly higher. Because of the missing additional photons from the back side, the perovskite top cell needs to transmit more light into the silicon subcell to ensure current-matching conditions. For a bandgap of around 1.65 eV, both junctions generate roughly equal current densities.

Figure 7 shows the simulated energy yield over the two days (August 26, 2019 and February 15, 2020) of available data for one module of mono- or bifacial silicon cells (green), 2-terminal (blue) and 4-terminal (orange) perovskite/silicon tandem cells for different perovskite bandgaps (in case of the tandems). The monofacial silicon cell yields around 3.3 kWh on these two days while the bifacial equivalent yields 3.9 kWh, an increase of roughly 20%. The energy yield of the monofacial 2-terminal tandem module strongly depends on the perovskite bandgap, with an optimal bandgap of 1.66 eV. The optimal bandgap of the bifacial 2-terminal tandem is shifted to 1.56 eV and an overall increased electrical yield is found. Overall, mono- and bifacial 4-terminal tandem cells show a lower dependence on the perovskite bandgap with the optimum at the maximum of the chosen perovskite bandgap range. The optimal bandgap does not change under bifacial operation. We choose a range of 1.5–1.7 eV because in this range high-quality perovskite materials have been demonstrated while perovskite cells with higher bandgaps can be difficult to manufacture.[36]

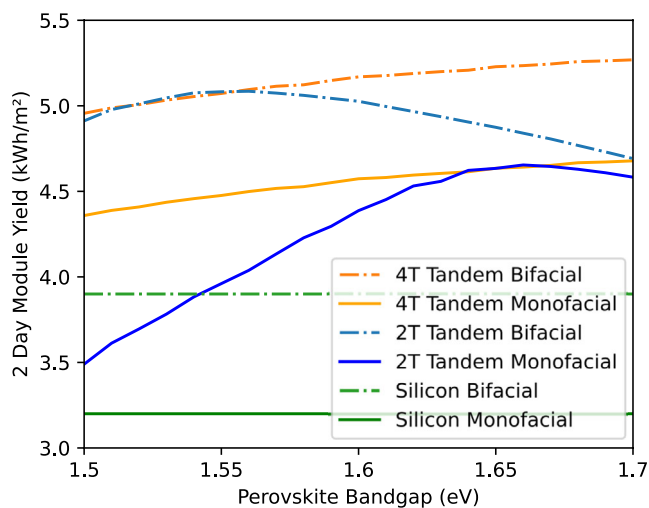At their individual optimal bandgap, 2-terminal tandem solar cells show a slightly higher module yield compared to the

corresponding 4-terminal configuration at the same bandgap. However, the 4-terminal configurations have a higher energy yield at the maximum bandgap. Please note that the results shown in Figure 7 should only be regarded as a rough estimation of optimum perovskite bandgaps. We regarded the EQE_{el} as a constant parameter in our simulations neglecting its dependence on temperature, injection, and particularly, the perovskite bandgap. This might lead to an underestimation of the tandem energy yield for lower-bandgap perovskites where much higher EQE_{el} values have been reported,[37] and to an overestimation of the yield when the tandem solar cells comprise wide-bandgap perovskite top cells, which often suffer from photo-induced phase segregation deteriorating the open-circuit voltage.[38] This might especially impact 4-terminal tandem solar cells where an optimum perovskite bandgap at the upper edge of the investigated range was found. For more detailed energy yield calculations the individual performance of the perovskite top cell in terms of EQE_{el} has to be considered.

The addition of a perovskite, wide-bandgap top cell atop a silicon bottom cell enables obtaining higher power conversion efficiencies owing to a reduction of thermalization losses of high energy photons. As this concept might also work for light impinging on the backside of the solar module, we also propose a triple-junction, 4-terminal perovskite/silicon-perovskite "sandwich" architecture. **Figure 8**a shows the schematic stack of this solar cell configuration. The top perovskite and the middle silicon cell are connected in series and form two electrical contacts (terminals) of the cell. The bottom perovskite is insulated by a layer of EVA, similar to the perovskite cell in the conventional 4-terminal tandem, and is connected with two separate terminals. The two top junctions will absorb similar photocurrent densities when the perovskite bandgap is chosen properly while the bottom perovskite will only absorb a fraction of the light due to the significantly lower irradiance at the back side of the module. Figure 8b shows the effect of the top and bottom perovskite bandgap and the 2-day energy yield. The effect of the top cell bandgap is much larger and an optimum is found at around 1.63 eV. The optimal bottom cell bandgap is found at the lower bound at 1.50 eV. It seems to be beneficial to absorb as much light as possible in the bottom perovskite junction. Figure 8c shows the calculated photocurrent density in the top-, middle- and bottom-junctions over the course of August 26, 2019 for a "sandwich" solar cell with a top and bottom cell bandgap of 1.63 and 1.50 eV, respectively. The photocurrent density of the top perovskite and the silicon junction is quite well matched, resulting in optimal utilization of the impinging light. In contrast, the bottom perovskite cell absorbs only a fraction of the photocurrent densities due to the lower irradiance at the back side of the module. Figure 8d shows the IV-curves of the "sandwich" at 1 pm on August 26, 2019. Due to the low intensity of light absorbed in the bottom perovskite junction, the open-circuit voltage is rather low, and therefore the power conversion efficiency is reduced.

Figure 7. Simulated two-day (August 26, 2019 and February 15, 2020) energy yield of one module for different solar cell technologies as function of the perovskite bandgap (in case of tandems). The geometrical parameters of the solar panel array as well as the albedo (60%) are identical to the parameters of the Jerusalem rooftop installation as specified in Table 1.

3.5. Discussion

In this final section, we compare the results and discuss the prospects of different cell designs. **Figure 9** shows the combined energy yield of the two sunny days (August 26, 2019 and
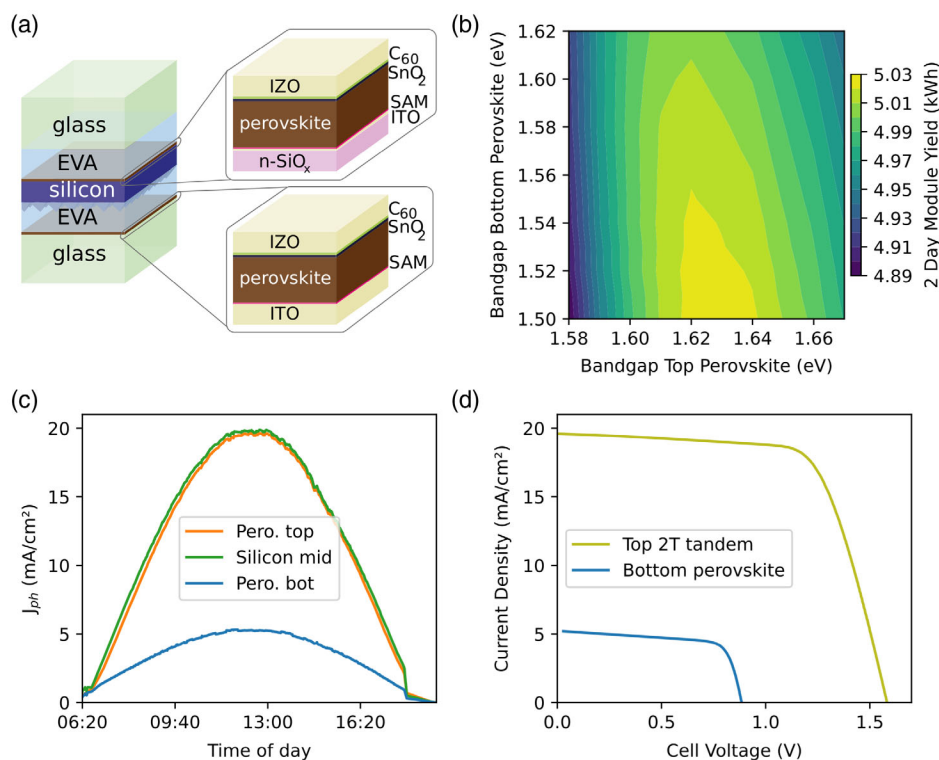
Figure 8. Simulation setup and results for 4-terminal sandwich configuration. a) Stack of the simulated "sandwich" solar cell. The upper perovskite and the silicon cell form a 2-terminal tandem, the lower perovskite is electrically independent with its own 2-connection terminals. b) Two-day energy yield for various bandgaps of the top (*x*-axis) and bottom (*y*-axis) perovskite. c) Absorbed photocurrent density J_{ph} over the course of August 26, 2019 for the three junctions of the device. d) Example *IV*-curves for August 26, 2019, 13:00. Because top perovskite and silicon subcells are connected in series they share one *IV*-curve as a tandem.
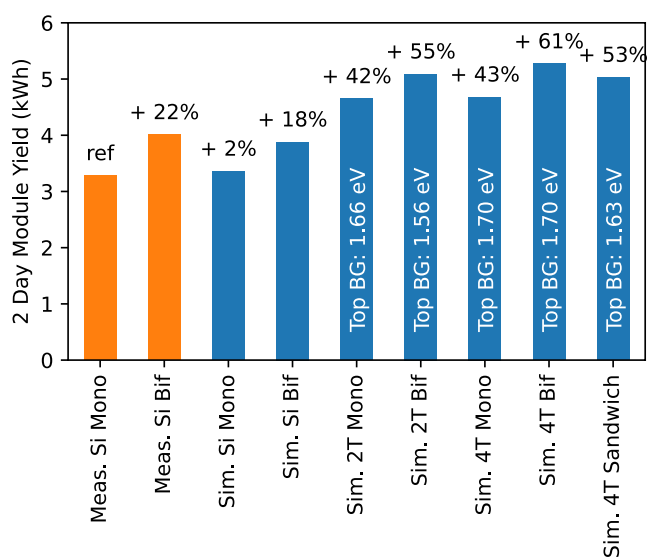

Figure 9. Two-day (August 26, 2019 and February 15, 2020) energy yield comparison of one module for all investigated solar cell architectures. The first two bars show the experimental result for mono and bifacial silicon solar cells. For all tandem solar cells the best performing perovskite bandgap was selected. The shown relative gains in percentage all refer to the experimental monofacial result.

February 15, 2020) with measured data for one module on the Jerusalem rooftop solar panel array installation, and with simulated estimates for different solar cell technologies. The first two bars show the measured energy yield of the monofacial and bifacial PERT silicon solar cell module. Compared to the monofacial module (reference) the bifacial module yielded 22% higher energy outputs. It has to be noted that the most common surfaces below bifacial solar power plants exhibit lower albedo values than 60% as in the case of the specific Jerusalem rooftop installation. Therefore, and considering the short timeframe of this study, the bifacial gain cannot be generalized and the +20% should be regarded as an upper bound for the bifacial energy yield gain. Simulated results for the silicon cells show similar numbers, however, the difference between the monofacial and the bifacial is lower, with only 16% gain due to bifaciality. We use the same cell parameters for the mono- and bifacial module, however, the *FF* of the bifacial cell seems to be higher (See Figures S5 and S6 in the Supporting Information). This results in an underestimation of the generated power and explains some of the differences between simulated and measured bifacial gain. Another factor can be found in the assumption of the model, where rows are infinitely wide and infinitely many rows are present. In the rooftop installation, however, there are only four rows with three modules each, where some light will shine in from the sides or the front, which is not considered by our model.

When switching to monofacial perovskite-on-silicon tandem technology, the results show an increase in the energy yield of 42%, which is significantly higher than the gain possible with silicon bifacial technology. This result is comparable with a study by Lehr et al.[16] who calculated around 40% increased energy yield for a monofacial tandem solar cell. The bifacial 2-terminal tandem is even able to produce 54% more energy than the silicon reference. This is a 13 p.p. increase with bifaciality, compared to the 16 p.p. from the simulated silicon cell results. This is in agreement with our earlier study[18] and findings by Onno et al.[13]. Because of the lower perovskite bandgap for current-matching in the bifacial tandem solar module, the voltage of the cell is also reduced. The lower cell voltage reduces the power conversion efficiency of light received at the front side compared to a monofacial tandem with a higher bandgap, and therefore the yield gain of 13 p.p. with bifaciality is the lowest for all considered technologies.

Because the perovskite and the silicon subcells are electrically independent in the 4-terminal configuration, the bifacial operation does not affect the consideration of the perovskite top cell bandgap. This results in a 43% and 61% higher energy yield for the mono- and bifacial 4-terminal tandem, respectively, an increase of 18 p.p. by bifacial operation. This shows that 4-terminal tandems can utilize bifacial operation slightly better than 2-terminal connections.

Finally, we discuss the results for the 4-terminal "sandwich," a design that includes two perovskite junctions with a silicon cell in between. Such a configuration is only sensible in bifacial operation because under monofacial operation no light would reach the bottom perovskite cell. Our results suggest that such a device does not improve the energy yield compared to conventional tandem devices. Both, the standard bifacial 2-terminal and 4-terminal tandem solar cells, show higher energy yields. The increased complexity and cost of an additional perovskite junction do not translate into higher energy gains. This is because of the low voltage of the bottom perovskite cell associated with the low light intensity at the back side of the solar cell module.

4. Conclusion

In this work, we presented measured and simulated results for a solar panel array installed on a rooftop in Jerusalem, Israel. Irradiance and solar cell performance data for two sunny days, one in summer, one in winter, were available. We used the experimental performance data of the PERT silicon solar cells to validate the different steps in our model chain. We validated the illumination on the front and back side of the model, the absorbed photocurrent based on optical simulations of the solar cell stack, and finally the electrical performance calculated from a temperature-dependent one-diode model to model the cells open-circuit voltage, FF, and power at maximum power point.

In this study, we confirm earlier findings, that bifacial operation significantly alters the ideal bandgap for 2-terminal tandem solar cells, favoring the potentially more stable lower perovskite bandgaps, while 4-terminal tandem solar cells only show a weak dependence on the bandgap.

Finally, we compared the measured and simulated energy yield of PERT silicon solar cells for two days, and calculated

the expected gain for a situation where the conventional silicon solar panels were replaced by 2-terminal and 4-terminal perovskite/silicon tandem solar cells in mono- and bifacial configuration at the same location. Assuming that current results for small-area perovskites cells can be scaled up in the future, monofacial 2- and 4-terminal tandems could result in 40–45% higher energy yields than monofacial silicon solar cells. Using bifacial tandem solar cells and albedo increasing measures can further increase the power output, with even 54–63% energy yield gain compared to a monofacial silicon solar module. A 4-terminal "sandwich" configuration was introduced, with two perovskite junctions surrounding one silicon cell in the center, but no additional gain was found. The low light intensity in the bottom perovskite possibly limits the performance and overall the device showed no gain compared to classical 2- or 4-terminal tandem cells.

Supporting Information

Acknowledgements

Conflict of Interest

The authors declare no conflict of interest.

Data Availability Statement

The data that support the findings of this study are available from the corresponding author upon reasonable request.

Keywords

[1] R. Kopecek, J. Libal, *Nat. Energy* **2018**, *3*, 443.
[2] T. S. Liang, M. Pravettoni, C. Deline, J. S. Stein, R. Kopecek, J. P. Singh, W. Luo, Y. Wang, A. G. Aberle, Y. S. Khoo, *Energy Environ. Sci.* **2019**, *12*, 116.

[3] *ITRPV, Technical Report, VDMA* **2021**, itrpv.vdma.org (accessed: July 2021).

[4] R. Kopecek, J. Libal, *Energies* **2021**, *14*, 2076, number: 8 Publisher: Multidisciplinary Digital Publishing Institute.

[5] A. Weselek, A. Ehmann, S. Zikeli, I. Lewandowski, S. Schindele, P. Högy, *Agron. Sustainable Dev.* **2019**, *39*, 35.

[6] G. M. Tina, F. Bontempo Scavo, L. Merlo, F. Bizzarri, *Appl. Energy* **2021**, *281*, 116084.

[7] T. Katsaounis, K. Kotsovos, I. Gereige, A. Basaheeh, M. Abdullah, A. Khayat, E. Al-Habshi, A. Al-Saggaf, A. E. Tzavaras, *Renewable Energy* **2019**, *143*, 1285.

[8] D. Berrian, J. Libal, *Prog. Photovoltaics Res. Appl.* **2020**, *28*, 609.

[9] S. A. Pelaez, C. Deline, S. M. MacAlpine, B. Marion, J. S. Stein, R. K. Kostuk, *IEEE J. Photovoltaics* **2019**, *9*, 82, conference Name: IEEE Journal of Photovoltaics.

[10] C. W. Hansen, J. S. Stein, C. Deline, S. MacAlpine, B. Marion, A. Asgharzadeh, F. Toor, in *2016 IEEE 43rd Photovoltaic Specialists Conf. (PVSC)*, IEEE, Portland, OR, USA **2016**, pp. 0138–0143, https://doi.org/10.1109/PVSC.2016.7749564.

[11] B. Marion, S. MacAlpine, C. Deline, A. Asgharzadeh, F. Toor, D. Riley, J. Stein, C. Hansen, in *2017 IEEE 44th Photovoltaic Specialist Conf. (PVSC)*, IEEE, Piscataway, NJ **2017**.

[12] J. E. Castillo-Aguilella, P. S. Hauser, *IEEE Access* **2016**, *4*, 498, conference Name: IEEE Access.

[13] A. Onno, N. Rodkey, A. Asgharzadeh, S. Manzoor, Z. J. Yu, F. Toor, Z. C. Holman, *Joule* **2020**, *4*, 580.

[14] A. Al-Ashouri, E. Köhnen, B. Li, A. Magomedov, H. Hempel, P. Caprioglio, J. A. Márquez, A. B. M. Vilches, E. Kasparavicius, J. A. Smith, N. Phung, D. Menzel, M. Grischek, L. Kegelmann, D. Skroblin, C. Gollwitzer, T. Malinauskas, M. Jošt, G. Matič, B. Rech, R. Schlatmann, M. Topič, L. Korte, A. Abate, B. Stannowski, D. Neher, M. Stolterfoht, T. Unold, V. Getautis, S. Albrecht *Science* **2020**, *370*, 1300.

[15] R. Schmager, M. Langenhorst, J. Lehr, U. Lemmer, B. S. Richards, U. W. Paetzold, *Opt. Express* **2019**, *27*, A507, publisher: Optical Society of America

[16] J. Lehr, M. Langenhorst, R. Schmager, F. Gota, S. Kirner, U. Lemmer, B. S. Richards, C. Case, U. W. Paetzold, *Sol. Energy Mater. Sol. Cells* **2020**, *208*, 110367.

[17] O. Dupré, A. Tuomiranta, Q. Jeangros, M. Boccard, P.-J. Alet, C. Ballif, *IEEE J. Photovoltaics* **2020**, *10*, 714.

[18] K. Jäger, P. Tillmann, E. A. Katz, C. Becker, *Sol. RRL* **2021**, *5*, 2000628.

[19] M. De Bastiani, A. J. Mirabelli, Y. Hou, F. Gota, E. Aydin, T. G. Allen, J. Troughton, A. S. Subbiah, F. H. Isikgor, J. Liu, L. Xu, B. Chen, E. Van Kerschaver, D. Baran, B. Fraboni, M. F. Salvador, U. W. Paetzold, E. H. Sargent, S. De Wolf, *Nat. Energy* **2021**, *6*, 167.

[20] K. Jäger, P. Tillmann, C. Becker, *Opt. Express* **2020**, *28*, 4751.

[21] P. Tillmann, K. Jäger, C. Becker, *Sustainable Energy Fuels* **2019**, *4*, 254.

[22] S. A. Pelaez, C. Deline, B. Marion, B. Sekulic, J. Parker, B. McDanold, J. S. Stein, in *Conf. Record of the IEEE Photovoltaic Specialists Conf.*, Vol. *2020-June*, IEEE, Calgary, AB, Canada, ISBN 9781728161150, ISSN 01608371, **2020**, pp. 1757–1759, https://doi.org/110.1109/PVSC45281.2020.9300379.

[23] N. Riedel-Lyngskær, D. Berrian, D. Alvarez Mira, A. Aguilar Protti, P. B. Poulsen, J. Libal, J. Vedde, *Appl. Sci.* **2020**, *10*, 8487.

[24] R. E. Bird, C. Riordan, *J. Clim. Appl. Meteorol.* **1986**, *25*, 87.

[25] R. Santbergen, T. Meguro, T. Suezaki, G. Koizumi, K. Yamamoto, M. Zeman, *IEEE J. Photovoltaics* **2017**, *7*, 919.

[26] K. Jäger, L. Korte, B. Rech, S. Albrecht, *Opt. Express* **2017**, *25*, A473.

[27] D. P. McMeekin, G. Sadoughi, W. Rehman, G. E. Eperon, M. Saliba, M. T. Hörantner, A. Haghighirad, N. Sakai, L. Korte, B. Rech, M. B. Johnston, L. M. Herz, H. J. Snaith, *Science* **2016**, *351*, 151.

[28] U. Rau, *Phys. Rev. B* **2007**, *76*, 085303.

[29] M. T. Hörantner, H. J. Snaith, *Energy Environ. Sci.* **2017**, *10*, 1983.

[30] B. Chen, S.-W. Baek, Y. Hou, E. Aydin, M. D. Bastiani, B. Scheffel, A. Proppe, Z. Huang, M. Wei, Y.-K. Wang, E.-H. Jung, T. G. Allen, E. V. Kerschaver, F. P. G. de Arquer, M. I. Saidaminov, S. Hoogland, S. D. Wolf, E. H. Sargent, *Nat. Commun.* **2020**, *11*, 1257.

[31] Y. Hou, E. Aydin, M. De Bastiani, C. Xiao, F. H. Isikgor, D. J. Xue, B. Chen, H. Chen, B. Bahrami, A. H. Chowdhury, A. Johnston, S. W. Baek, Z. Huang, M. Wei, Y. Dong, J. Troughton, R. Jalmood, A. J. Mirabelli, T. G. Allen, E. Van Kerschaver, M. I. Saidaminov, D. Baran, Q. Qiao, K. Zhu, S. De Wolf, E. H. Sargent, *Science* **2020**, *367*, 1135.

[32] F. Sahli, J. Werner, B. A. Kamino, M. Bräuninger, R. Monnard, B. Paviet-Salomon, L. Barraud, L. Ding, J. J. Diaz Leon, D. Sacchetto, G. Cattaneo, M. Despeisse, M. Boccard, S. Nicolay, Q. Jeangros, B. Niesen, C. Ballif, *Nat. Mater.* **2018**, *17*, 820.

[33] R. Santbergen, M. R. Vogt, R. Mishima, R. Mishima, M. Hino, H. Uzu, D. Adachi, K. Yamamoto, M. Zeman, O. Isabella, *Opt. Express* **2022**, *30*, 5608.

[34] M. Jošt, B. Lipovšek, B. Glažar, A. Al-Ashouri, K. Brecl, G. Matič, A. Magomedov, V. Getautis, M. Topič, S. Albrecht, *Adv. Mater.* **2020**, *10*, 2000454.

[35] A. Rohatgi, K. Zhu, J. Tong, D. H. Kim, E. Reichmanis, B. Rounsaville, V. Prakash, Y. W. Ok, *IEEE J. Photovoltaics***2020**, *10*, 417.

[36] M. Jošt, L. Kegelmann, L. Korte, S. Albrecht, *Adv. Mater.* **2020**, *10*, 1904102.

[37] J. J. Yoo, G. Seo, M. R. Chua, T. G. Park, Y. Lu, F. Rotermund, Y. K. Kim, C. S. Moon, N. J. Jeon, J. P. Correa-Baena, V. Bulović, S. S. Shin, M. G. Bawendi, J. Seo, *Nature* **2021**, *590*, 587.

[38] E. L. Unger, L. Kegelmann, K. Suchan, D. Sörell, L. Korte, S. Albrecht, *J. Mater. Chem. A* **2017**, *5*, 11401.